JPE Journal of Photonics for Energy

RESEARCH PAPER

# Zero-energy switchable radiative cooler for enhanced building energy efficiency

**Changhao Chen, XuSheng Xia,* JiaQi Hu, Ruichen Song, Bin Li, Hengren Hu,**
**YunQi Peng, and Zhilin Xia**
Wuhan University of Technology, Material Science and Engineering, Wuhan, China

**ABSTRACT.** Fossil fuel consumption for heating and cooling represents a considerable portion, approximately half, of the world's total energy use, thereby presenting a substantial challenge in diminishing dependence on these energy sources. Our study presents the design and fabrication of a zero-energy switchable radiative cooler (ZESRC) to address the global climate crisis by reducing energy consumption within buildings. ZESRC utilizes a simple morphology-driven method that exploits materials' differing thermal expansion coefficients, enabling a seamless switch between cooling and heating modes at any preset temperature point, enabling superior adaptive thermal management. Field experiments demonstrate that, relative to ambient temperature, ZESRC usage results in a maximum temperature decrease of 7.1°C during summer and a maximum increase of 7.5°C in winter. Furthermore, we developed an energy-efficiency map for different climate zones, showing the ZESRC's superiority over devices with only solar heating or radiative cooling, cutting building energy use by 14.3%. The results underscore the ZESRC's capability for net-zero energy consumption, significantly advancing global energy conservation and the 2050 net-zero carbon goal.

[DOI: 10.1117/1.JPE.14.028501]

**Keywords:** radiative cooling; temperature-responsive; thermal management; building energy-saving; switchable radiative cooling technology

Paper 23053G received Nov. 27, 2023; revised Jan. 20, 2024; accepted Jan. 26, 2024; published Feb. 26, 2024.

## 1 Introduction

The global climate crisis is a pressing challenge for humanity today. Energy-related greenhouse gas emissions significantly worsen the climate crisis.[1,2] In developed countries, the building sector accounts for about 40% of total energy use, surpassing the industrial and transportation sectors. Notably, heating, ventilation, and air conditioning systems account for half of the building sector's energy use.[3,4] The widespread use of air conditioning for building thermal management has considerably increased electricity demand. Moreover, the widespread utilization of these systems results in the significant emission of greenhouse gases and ozone-depleting substances, exacerbating global warming.[5] Therefore, developing effective thermal management technologies that are high-performance, energy-efficient, and capable of net zero energy use is crucial. Advancements in these technologies are vital to reduce dependence on fossil fuels and decrease greenhouse gas emissions.

Radiative cooling is emerging as a promising zero-energy thermal management solution to reduce fossil fuel use and environmental pollution. This technology is attracting significant interest for sustainable energy practices.[6] Radiative cooling allows for efficient cooling without extra

---

*Address all correspondence to XuSheng Xia, xsxia@whut.edu.cn

1947-7988/2024/$28.00 © 2024 SPIE

energy input or greenhouse gas emissions, offering a sustainable solution. High-efficiency radiative cooling depends on optimizing material spectral selectivity. Using a tailored electromagnetic spectrum design can greatly improve the reflectivity of radiative cooling materials in the solar spectrum band (0.3 to 2.5 $\mu$m) and their emissivity in the atmospheric window band (8 to 13 $\mu$m). This modification regulates the radiative balance between the solar heat source (5800 K) and the cosmic deep space cold sink (3 K).[7,8] Recently, diverse designs for high-performance radiative cooling have been introduced, such as multilayer photonic films,[9–11] insulating aerogels,[12–14] white paints,[15–17] wood,[18,19] textiles,[20–22] and particle-embedded polymers.[23–25] These have been extensively applied in important areas, such as atmospheric water harvesting,[26,27] personal thermal management,[28,29] thermoelectric materials,[30,31] photovoltaic power generation,[32,33] and building energy conservation.[34,35]

Despite its significant cooling potential, radiative cooling must address the varying cooling demands of terrestrial structures like buildings, which operate under changing weather conditions. Such variations can result in overcooling, particularly during nighttime and winter months, thereby escalating heating expenses and possibly negating the energy savings achieved during warmer times. Consequently, advancing switchable radiative cooling (SRC) technology, which adapts to changing environmental conditions, is critical.

Researchers are working to overcome the fixed regulation limits of radiative cooling and to expand its applications; extensive studies are being undertaken on SRC technology. For example, Ke et al. developed a reconfigurable surface allowing for dynamic sequence changes, which enable spectral selectivity and broadband modulation. This active SRC system shows great potential for customizable modes and programmable thermal management.[36] Li et al. proposed a polymer radiative cooling system with an electric motor to adjust film curvature for heating and cooling transitions as needed. This innovation enables thermal regime modulation to meet dynamic thermal management needs.[37] Active SRC technologies have made mode transitions smoother, serving varied heating, and cooling needs for comfort. However, these systems depend on extra mechanical and electrical energy, preventing true zero-energy adaptive functionality. Recent research has integrated temperature-responsive materials into passive radiative cooling systems, edging closer to complete zero-energy adaptive thermal management.[38] Vanadium dioxide ($VO_2$), a phase-change metal oxide, exhibits reversible, temperature-dependent dielectric properties with distinct variations between its metallic and insulating states. Despite significant research interest due to its unique properties, $VO_2$'s high phase transition temperature of 68°C limits its suitability for building applications.[39–42] Tang et al. have innovated a temperature-adaptive radiative coating. They achieved this by doping $VO_2$ with tungsten, effectively lowering its phase transition point to room temperature. This innovation enables zero-energy consumption and efficient thermal regulation in buildings year-round.[40] The high cost and complex preparation of $VO_2$, along with the difficulty in controlling its temperature switching point, significantly impede its mass production and broad application. Consequently, creating a process-simple, zero-energy SRC device with an easily adjustable temperature switch point remains a significant challenge.

In this study, we designed and built the zero-energy switchable radiative cooler (ZESRC), an innovative solution designed for efficient thermal management without necessitating energy consumption. The ZESRC operates on a novel, morphology-driven approach, utilizing materials with varying thermal expansion coefficients to enable a dynamic response to temperature changes. This design allows for a seamless transition between cooling mode ($\alpha_{0.28\text{ to }0.78\ \mu\text{m}}$ of 0.2% and $\varepsilon_{8\text{ to }13\ \mu\text{m}}$ of 96.2%) and heating mode ($\alpha_{0.28\text{ to }0.78\ \mu\text{m}}$ of 33.2% and $\varepsilon_{8\text{ to }13\ \mu\text{m}}$ of 0.3%) at any preset temperature point to address diverse thermal management needs in various scenarios. Field tests of ZESRC devices showed a maximum daytime temperature drop of 7.1°C in summer and a maximum increase of 7.5°C in winter. We also computed the energy efficiency of buildings in most major Chinese cities and developed an energy-saving map for different climate zones. The map indicates that our ZESRC surpasses traditional solar heating or cooling devices, saving an average of 14.3% in building energy consumption for heating and cooling. These results suggest that ZESRC can adjust the cooling efficiency of buildings dynamically, maintaining thermal comfort. The ZESRC shows significant potential for energy conservation, which is crucial for achieving the 2050 net-zero carbon goal.

## 2 Experimental Section

### 2.1 Materials and Preparation of ZESRC

Zirconium dioxide nanoparticles ($ZrO_2$ NPs), poly(methyl methacrylate) (PMMA), and $N,N$-dimethylacetamide (DMAc) were purchased from vendors. 3M VHB tape, polyethylene (PE) film, and copper foil tape were purchased from online stores.

The radiative cooling layer was created using a nonsolvent-induced phase separation technique. The preparation involved dissolving PMMA in DMAc, followed by stirring in a 60°C water bath for 2 h until fully dissolved. $ZrO_2$ NPs were then added, and the mix was ultrasonicated for 1 h to produce a uniform slurry. This results in a precursor solution with a PMMA to DMAc to $ZrO_2$ mass ratio of 1:8:1. The slurry is poured into a custom glass mold and submerged in deionized water for 12 h to complete phase separation. The sample is then removed and air-dried to form the radiative cooling layer. The solar heating layer uses a direct application of copper foil. For the temperature-sensitive actuator layer, under any preset switch temperature, a PE film is laid out on a smooth plane, and a copper foil with a backing adhesive is gradually adhered to the PE film using a glass rod. This simple method completes the assembly of the temperature-sensitive actuator layer, and the preset switch temperature can change with the ambient temperature. The temperature-sensitive actuator and radiative cooling layers are joined at the top with narrow VHB tape. The excellent durability and adhesive properties of VHB tape in extreme environments contribute to the long-term usability of ZESRC devices.[43] Samples for this experiment were prepared at a laboratory temperature of ~20°C, with each sample measuring 5 cm × 8 cm.

### 2.2 Characterization and Measurements

#### 2.2.1 *Spectral characteristics and morphology of ZESRC*

We used a UV-visible-near infrared spectrophotometer (Lambda 750 S) with an integrating sphere and a Fourier transform infrared spectrometer (Thermo Scientific Nicolet iS20) with an integrating sphere to measure the ZESRC's spectral properties in different modes. Solar reflectance ($\overline{R}_{\text{solar}}$) and long-wave infrared emissivity ($\overline{\varepsilon}_{\text{LWIR}}$) are vital for evaluating the ZESRC's performance, with calculation methods detailed in Note 2 in the Appendix section. A scanning electron microscope (TESCAN MIRA LMS) was used to analyze the ZESRC's surface morphology.

#### 2.2.2 *Bending angle testing of ZESRC*

To measure the bending angle, the actuator is placed on a copper plate with its short edge fixed and then put into an environmental chamber that regulates temperature with heated or cooled air. The chamber temperature is set manually using a control panel, with bending angle measurements conducted at 15°C, 20°C, 25°C, 30°C, and 35°C. Photos are taken, and angles are recorded when the actuator's bending angle stabilizes at each set temperature. For infrared imaging, the ZESRC and a standard RC are placed on a heating plate set to 50°C, and an infrared gun (Testo865) captures the ZESRC's temperature-driven switching process.

#### 2.2.3 *Measurement of linear thermal expansion coefficient*

We assessed the linear thermal expansion coefficients for PE and copper foil using the Netzsch TMA 402 F3 Thermal Mechanical Analyzer. Each film was cut into a 20 mm × 3 mm rectangle and attached to two hooks. A small force of 0.05 N was applied to the film to keep it straight during testing. The test covered a temperature range of 15°C to 35°C, scanning at a rate of 1°C/ min.

#### 2.2.4 *Outdoor experimental method*

The test sample was placed in an experimental box made of polystyrene foam plastic, with the outer surface covered with aluminum foil to reflect sunlight. The top of the experimental box was sealed with PE film, and the box was placed on a rack 1 m above the ground to isolate ground heat conduction and suppress nonradiative heat exchange effects on the test sample, such as sunlight absorption and air convection. A multichannel temperature tester (JK808) was used to monitor the temperature changes of the sample. A louver box was used to record environmental temperature data, and a weather station was used to record weather data, such as solar radiation intensity, relative humidity, and wind speed. The outdoor experimental setup is shown in Fig. 9.

## 3 Results and Discussion

### 3.1 Conceptual Design of ZESRC

Fig. 1(a) depicts the ideal ZESRC comprising three layers: a radiative cooling layer at the bottom, a temperature-sensitive actuator in the middle, and a solar heating layer on top. The ZESRC employs a temperature-sensitive actuator for thermal management, which enables switching between heating and cooling modes at a preset temperature threshold determined by ambient conditions. The ideal spectrum corresponding to each mode is depicted in Fig. 1(b). In cold environments, such as winter, the ZESRC automatically activates the heating mode, with the actuator layer spreading the solar heating layer across the interface. By day, the solar heating layer absorbs solar radiation highly, converting it into thermal energy and at night the solar

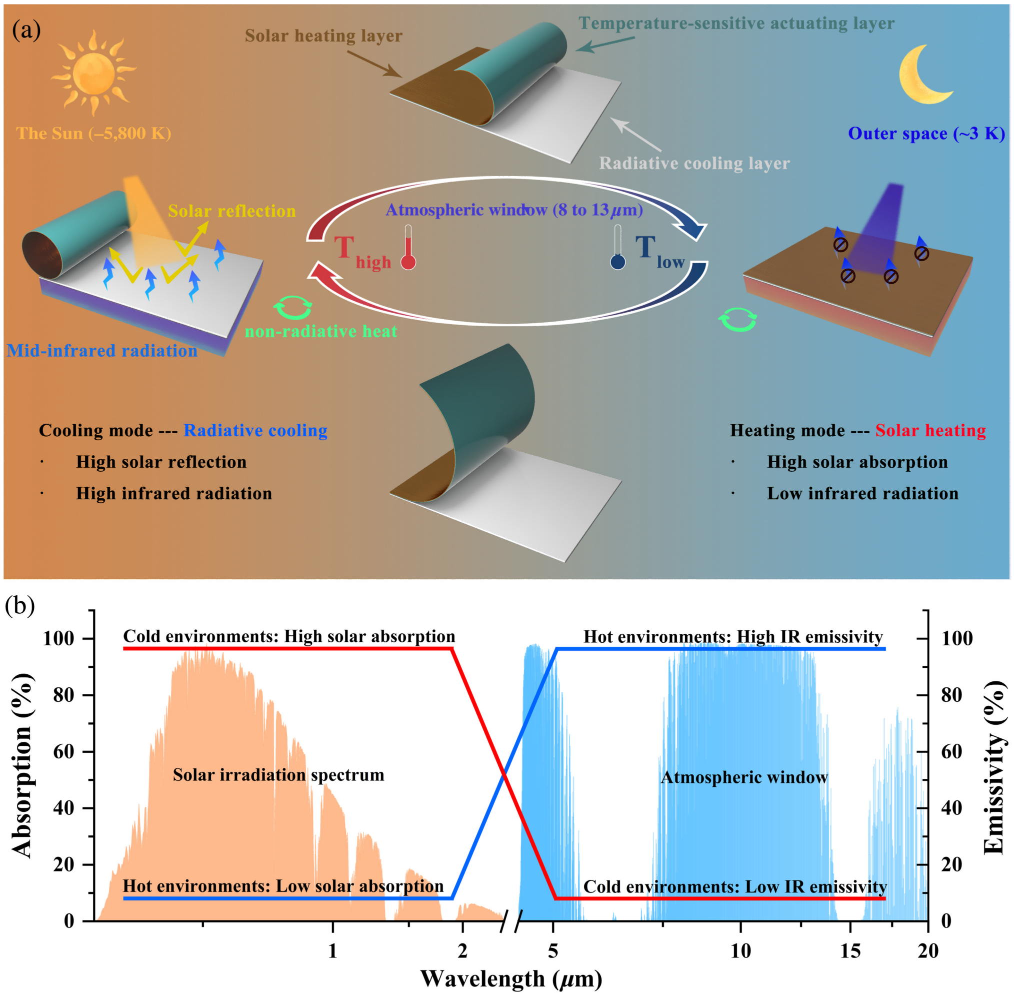

**Fig. 1** Design principle of ZESRC. (a) Schematic representation of the ZESRC automatically switching modes with temperature changes. The left image illustrates the cooling mode under high temperatures, whereas the right image depicts the heating mode under low temperatures. (b) The ideal spectral properties of ZESRC when in cooling and heating modes.

heating layer's low mid-infrared emissivity significantly cuts thermal radiation loss. In high temperature conditions, such as summer, the ZESRC automatically enters cooling mode, retracting the solar heating layer to expose the radiative cooling layer fully. The radiative cooling layer is characterized by minimal solar absorption and maximal emissivity within the atmospheric window range, theoretically enabling it to achieve continuous cooling below ambient temperatures. However, it is essential to note that the actual attainment of consistent subambient temperatures not only depends on the design of the cooling layer but is also significantly influenced by specific climatic conditions.[44] Even under ideal circumstances, a radiative cooling layer, optimized for low solar absorption and high emissivity, may exhibit varying cooling efficiencies in different climatic scenarios. Therefore, while the layer's fundamental properties provide the potential for subambient cooling, its real-world effectiveness must be evaluated considering ambient temperature and other relevant climatic factors.

The automatic switching mechanism is based on the response of the ZESRC's actuator layer to environmental temperature. The system uses the differential thermal expansion properties of its materials for responsive actuation that adapts to temperature fluctuations. High-linear thermal expansion coefficient PE ($\sim 10^{-4}$) is used in the actuator layer to enable shape changes in response to temperature changes. When exposed to higher temperatures, the PE expands thermally. A copper foil layer with a lower thermal expansion coefficient ($\sim 10^{-5}$) is laminated to the PE, creating a synergistic bilayer that enhances the expansion response. This design capitalizes on differential thermal expansion for effective actuation. In the design, the copper foil top layer serves as both the solar heating element and an inert material that deforms with temperature in order to limit the thermal expansion of the PE with temperature.

When PE and copper foil are bonded together at a certain ambient temperature, they adhere firmly and maintain a perfectly flat alignment due to the adhesive force. As the temperature increases, due to the linear thermal expansion coefficient of copper foil being much smaller than that of PE (as shown in Fig. 6), curling occurs from the PE side toward the copper foil side. This occurs because as the temperature rises, the deformation of PE is much greater than that of the thermally inert copper foil. The thermal mismatch caused by the difference in expansion leads the side with greater deformation to bend toward the side with less deformation. Fixing one end, the temperature increase prompts the driving layer to curl the initially flat solar heating layer toward the fixed end, maximizing exposure of the radiative cooling layer beneath, thereby enabling the shift from heating to cooling mode. As the temperature decreases, the solar heating layer uncoils and extends to cover the radiative cooling layer, facilitating a transition from cooling to heating mode. The observed characteristics imply that the bonding temperature of PE and copper foil during preparation marks the temperature switching point of the temperature-sensitive actuator. Consequently, adjusting the fabrication temperature facilitates easy modification of the temperature-sensitive actuator's preset switching point.

In summary, our ZESRC effectively reduces the overcooling associated with standard radiative cooling materials in cold climates, thus minimizing energy waste. Since temperature regulation is the ultimate aim of thermal management, temperature-responsive devices represent a superior strategy for consistent temperature control. Unlike electric or manual control methods for radiative cooling, our continuous temperature control strategy offers a genuinely zero-energy adaptive solution. This study utilizes material thermal expansion differences for a straightforward and practical actuation method, switching between heating and cooling modes at any preset temperature.

### 3.2 Bending Performance of the Temperature-Sensitive Actuating Layer

The bending performance of the actuating layer is key to the adaptive thermal management of the ZESRC, which operates without additional energy. We measured the bending angles of temperature-sensitive layers made from PE and copper foil at various thicknesses and temperatures in an environmental chamber. To identify the PE film thickness with optimal bending at temperatures between 15°C and 35°C, we combined a 20 $\mu$m copper foil with PE films of 30, 50, 80, and 100 $\mu$m thicknesses. These samples were labeled PE30, PE50, PE80, and PE100, respectively. We tested how different PE thicknesses affected the bending performance of the actuating layer. Figure 7 shows that the 50 $\mu$m PE layer achieved the highest bending angle among the samples at temperatures from 15°C to 35°C. This suggests that PE50 has the best actuating performance of the tested thicknesses. Therefore, the 50 $\mu$m PE actuator was chosen for further study. We investigated the effects of different copper thicknesses (20, 30, 50, and 80 $\mu$m) on the bending performance, keeping the PE thickness constant at 50 $\mu$m. The copper layers were designated Cu20, Cu30, Cu50, and Cu80. Figures 2(a) and 2(b) illustrate that all four samples had bending angles close to zero below the 20°C threshold. With increasing ambient temperature, the bending angles rose stepwise, showing a roughly linear relationship. The results showed a nonmonotonic trend: bending angles increased with thickness up to a point, then decreased. Cu30 showed the best bending, reaching a maximum angle of 420 deg at 35°C.

We examined the variation in bending angle of the optimal Cu30 sample with temperature during a single heating and cooling cycle, as depicted in Fig. 2(c). Observations reveal no significant temperature hysteresis in the angle, aligning closely with theoretical calculations. Specific theoretical calculations are detailed in Note 1 in the Appendix section. Figure 2(d)

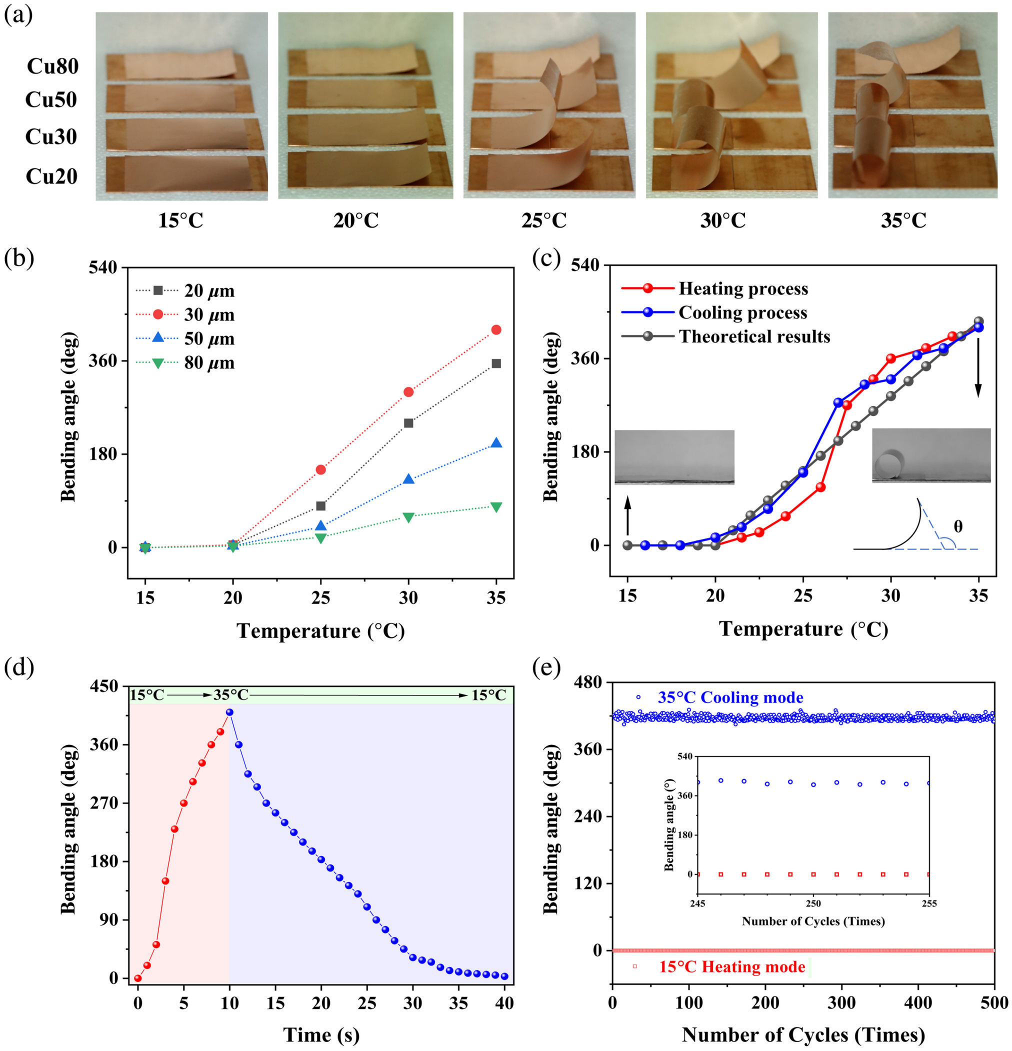

**Fig. 2** Bending performance of temperature-sensitive actuating layers. (a) Optical images of temperature-sensitive actuators with different copper foil thicknesses at a PE thickness of 50 $\mu$m under varying environmental temperatures. (b) The bending angles of temperature-sensitive actuators with different copper foil thicknesses at different environmental temperatures. (c) The bending angle and optical images of the temperature-sensitive actuator (Cu30) with the best bending performance during heating cycles as temperature changes, along with theoretical calculation results. (d) The change of bending angle over time for the temperature-sensitive actuator (Cu30) with the best bending performance during heating and cooling processes. (e) The cyclic stability of the temperature-sensitive actuator (Cu30) with the best bending performance more than 500 cycles.

shows our actuator layer switched from 15°C to 35°C, with the bending angle going from zero to maximum in just 10 s. Additionally, when transitioning from a high temperature of 35°C to a low temperature of 15°C, the bending angle of the actuator layer recovers from its maximum value to zero within 30 s. This demonstrates that the copper foil heating layer also automatically and rapidly returns to its initial state as the temperature decreases. Such rapid response proves the actuator's suitability for zero-energy, switchable radiative coolers, ensuring its rapid adaptability to temperature fluctuations. Figure 2(e) shows that during the heating process from 15°C to 35° C, the actuator transitions from being spread out to coiled, and during the cooling process from 35°C to 15°C, the actuator uncoils back to its spread state. After 500 temperature cycles of this heating and cooling, the actuator layer still maintains its ability to switch between its maximum and minimum bending angles, demonstrating excellent cyclic stability. This outstanding cyclic stability meets the demands for long-term practical use, with consistent bending performance proving this point.

### 3.3 Spectral Design of ZESRC

The adaptability of the ZESRC hinges on a multifunctional electromagnetic spectrum, facilitating the shift between heating and cooling modes. In designing the cooler's heating layer, we use copper foil as both the inert layer for the temperature-sensitive actuator and to exploit its high ultraviolet-visible (UV-VIS) absorption and long-wave shielding for minimal infrared absorption. When exposed to sunlight, the copper foil heats by absorbing a high amount of UV-VIS light, converting light to thermal energy. Furthermore, copper foil's high thermal conductivity facilitates the rapid and uniform transfer of heat, ensuring even temperature distribution. These attributes make copper foil highly suitable for widespread use as a solar heating layer. The cooling mode of the ZESRC uses a radiative cooling layer composed of PMMA mixed with $ZrO_2$ NPs, the microscopic morphology of the radiative cooling layer is demonstrated as shown in Figs. 3(a)–3(c). PMMA, a prevalent and economical polymer, is well-suited for high-performance radiative cooling applications.[45] PMMA is transparent in the solar spectrum with a refractive index of 1.49, considerably lower than the 2.2 index of $ZrO_2$ NPs from the visible to near-infrared ranges. The PMMA and $ZrO_2$ NPs mix, with a refractive index difference of 0.71, creates a stark transition at the interface, essential for effectively scattering solar radiation in the composite material. Figure 3(d) displays the calculated scattering efficiency of $ZrO_2$ NPs of various sizes in a PMMA matrix. An increase in $ZrO_2$ NPs diameter correlates with a redshift in the scattering peak. When the $ZrO_2$ NPs reach about 0.4 $\mu$m in diameter, they scatter solar radiation highly efficiently, minimizing absorption. In the experiment, the particle size distribution of zirconia is shown in Fig. 10. Figures 3(e) shows the ATR-FTIR measured absorption spectrum, indicating strong infrared absorption. This strong infrared absorption is due to the C–O–C group vibrations in PMMA, occurring within a wavenumber range of 770 to 1250 $\mathrm{cm}^{-1}$, aligning with 8 to 13 $\mu$m wavelengths. This range aligns with the atmospheric transparency window, allowing for efficient radiative heat exchange with the cold outer space through the significant infrared spectral features presented. These properties enable the layer to scatter solar light effectively and exchange heat efficiently with the cold of space via the atmospheric window. Consequently, the radiative cooling layer composed of PMMA and $ZrO_2$ NPs exhibits exceedingly high solar reflectance ($R_{\mathrm{Solar}}$) and long-wave infrared emissivity ($\varepsilon_{\mathrm{LWIR}}$), laying a robust foundation for achieving efficient, all-weather radiative cooling. Furthermore, our research investigated the impact of both the thickness and nanoparticle composition of the radiative cooler on its spectral response and mechanical properties, detailed in Figs. 11–13.

Integrated into the solar heating layer and temperature-sensitive actuating layer, the copper foil absorbs solar light efficiently and quickly converts it to thermal energy, enabling fast and uniform heat distribution. Upon reaching the preset switching temperature point, the temperature-sensitive actuating layer deforms and curls to expose the radiative cooling layer beneath, which reflects sunlight and facilitates efficient cooling. This feature allows the device to alternate between a heating mode with 33.2% absorption and 0.3% emissivity ($\alpha_{0.28\text{ to }0.78\ \mu\mathrm{m}}$ and $\varepsilon_{8\text{ to }13\ \mu\mathrm{m}}$) and a cooling mode with 0.2% absorption and 96.2% emissivity ($\alpha_{0.28\text{ to }0.78\ \mu\mathrm{m}}$ and $\varepsilon_{8\text{ to }13\ \mu\mathrm{m}}$), surpassing mere adjustments in heating or cooling intensity, the spectral characteristics of the device are depicted in Figs. 3(f) and 14.

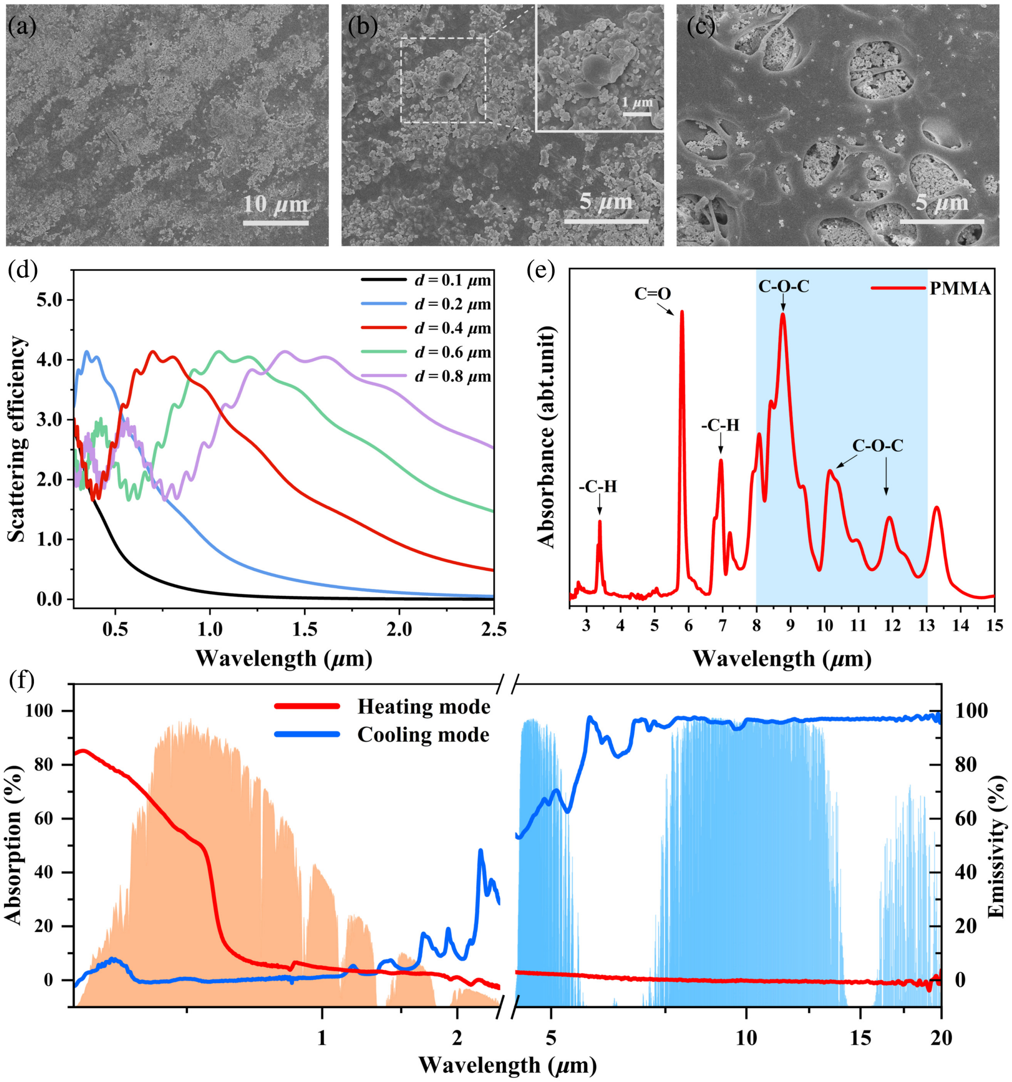

**Fig. 3** Structure and spectral characteristics of ZESRC. (a)–(c) Scanning electron microscope images of the radiative cooling layer. (d) Simulation of the scattering efficiency of $ZrO_2$ NPs in the solar light band with the change of particle diameter. (e) The absorption spectrum of PMMA is measured by ATR-FTIR spectroscopy. (f) Adaptive spectral graph of the ZESRC.

## 3.4 Thermal Management Performance of the ZESRC

### 3.4.1 *Indoor thermal management performance of ZESRC*

wTo effectively illustrate the intelligent switching and radiant thermal management capabilities of ZESRC indoors, we utilized an infrared thermometer and camera to capture thermal images of both ZESRC and a standard radiative cooler while they were heated on a hotplate. These images are presented in Fig. 4(a), and a demonstration is available in Video 1. The image's upper part shows the conventional radiative cooler for reference, and the lower part features the ZESRC. Initially, the ZESRC's radiative cooling layer is hidden by the solar heating layer, demonstrating its very low infrared emission. With increasing temperature, the temperature-sensitive actuating layer slowly curls the solar heating layer, revealing the radiative cooling layer until it is fully exposed and achieves high infrared emissivity. The infrared images clearly show the ZESRC's emissive property changes with temperature. The displayed adaptive thermal management proficiency provides a strong basis for future real-world outdoor experiments.

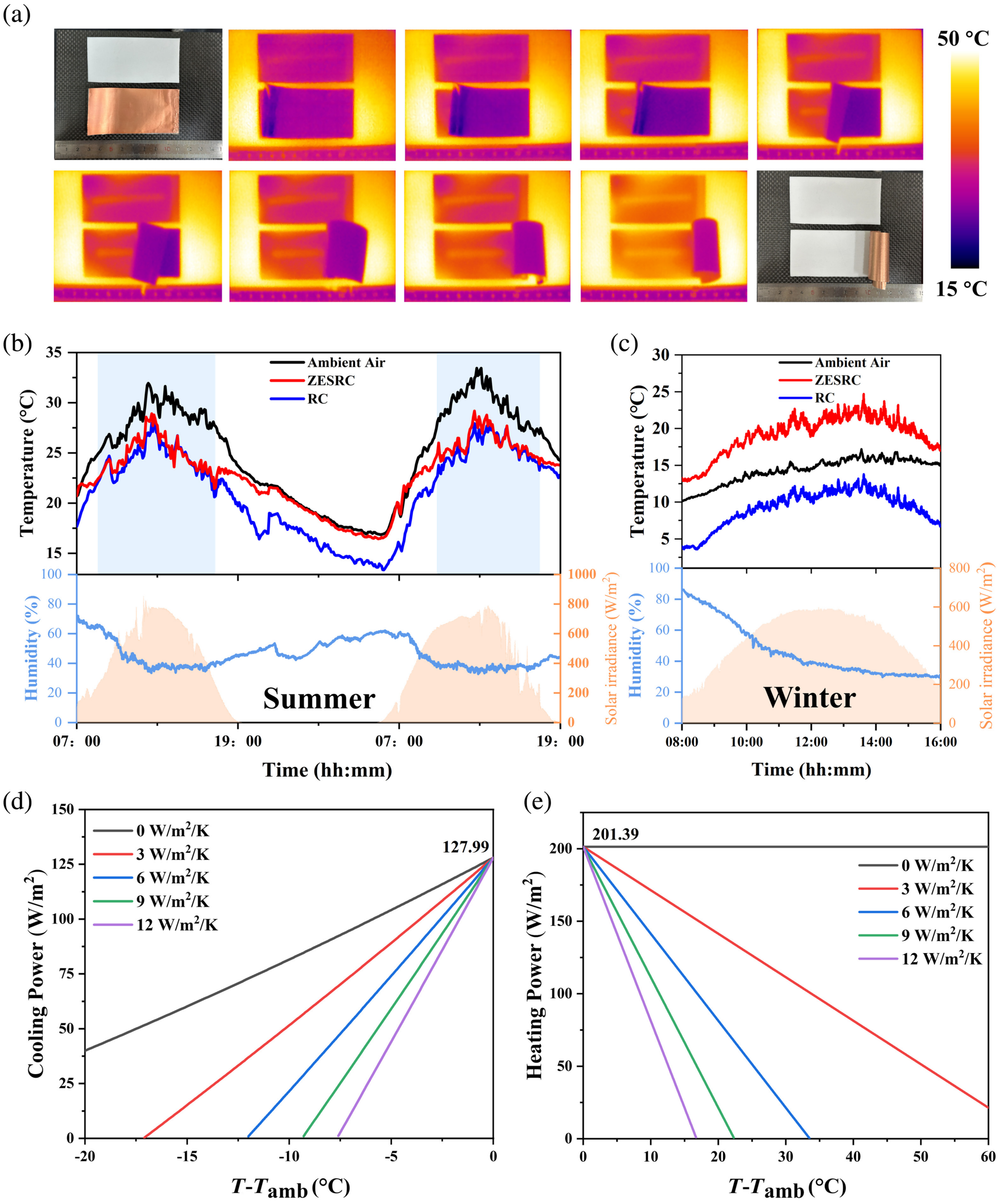

**Fig. 4** Comprehensive thermal management performance of the ZESRC. (a) Infrared imagery captured during the intelligent switching process of the ZESRC. (b) The real-time tracking of environmental temperature (black), the temperature of the ZESRC (red), and the temperature of a standalone radiative cooler (blue) during a continuous 36-h thermal management test conducted in real-world outdoor conditions; the corresponding environmental humidity and solar irradiance at each time point are depicted in the accompanying graph. (c) Winter real-world outdoor heat management test. (d) The calculation of net cooling power during the cooling mode operation. (e) The calculation of net heating power during the heating mode operation (Video 1, .mp4, 9.54 MB [URL: https://doi.org/10.1117/1.JPE.14.2.028501.s1]).

### 3.4.2 *Field test of ZESRC performance*

We performed outdoor tests on the roof of a Wuhan University of Technology building (30.52N, 114.34E) to assess the system's thermal management in real-world conditions, as illustrated in Fig. 9. To reduce nonradiative heat transfer effects on our samples, we placed them in a cavity insulated with thermal materials. We covered the cavity's exterior with reflective aluminum foil and the top with transparent, low-density PE film to limit nonradiative heat exchange losses. During a continuous 36-h field test conducted outdoors from 7:00 am on May 8, 2023, to

7:00 pm on May 9, 2023, the temperatures of the ZESRC and the pure radiative cooler (RC) were precisely measured with thermocouples, and the ambient temperature and relative humidity were accurately recorded using a Stevenson screen. Figure 4(b) shows that the pure radiative cooler (blue line), due to its reflective and emissive properties, kept an average temperature of 3.8°C below the ambient (black line) during peak solar radiation ($\sim$830 $\mathrm{W/m^2}$) and 46% relative humidity. This proves the pure radiative cooler's effectiveness in providing all-day cooling below ambient temperatures. It is noteworthy that if experimental tests are conducted in some arid geographic regions, the demonstrated cooling performance will be more pronounced. This is because radiative cooling is primarily achieved by emitting heat through a transparent atmospheric window from the material's surface to the cold space, and this process is greatly influenced by atmospheric humidity. In arid areas, the air humidity is lower, there is less water vapor in the atmosphere, and the transparency of the atmospheric window is greater, resulting in less obstruction to radiative transmission and thus higher efficiency of radiative cooling.[44,46] With increased solar radiation, the ZESRC's temperature (red line) also rises. Upon reaching the temperature-sensitive actuator's preset switching point, the ZESRC transitions from heating mode (low-infrared emission, high solar absorption) to cooling mode (high-infrared emission, low solar absorption). From 8:25 to 17:20 on May 8, the ZESRC was in cooling mode, with its temperature profile closely matching the pure radiative cooler's. From 14:00 to 17:00, the ZESRC's average temperature was 0.1°C lower than the pure radiative cooler's, confirming its full transition to cooling mode with a comparable cooling effect. Additionally, the ZESRC achieved a daytime temperature reduction of up to 7.1°C. When the ambient temperature drops below the temperature-sensitive actuator's preset switching point, the ZESRC automatically enters heating mode at night to keep warm, minimizing radiation to reduce heat loss. During the cold, sunless night from 19:00 to 6:00, the ZESRC automatically switches to heating mode. The ZESRC's average temperature was 2.8°C higher than the pure radiative cooler's, with a peak temperature increase of 4.6°C during the test period. To further validate ZESRC's thermal management efficacy in winter conditions, we conducted an outdoor test on November 16, 2023, as illustrated in Fig. 4(c). During winter daylight hours, ZESRC continuously heated as the environmental temperature fell below the temperature-sensitive actuator's preset switching point ($\sim$20°C). In this phase, ZESRC absorbed solar radiation, raising its average temperature by 4.7°C above the ambient level. At 13:30, it recorded a peak temperature increase of 7.5°C above the ambient temperature. Compared to the pure radiative cooler (RC), which cools effectively all day, ZESRC showed superior winter thermal management, averaging 9.8°C higher than the ambient temperature.

The outdoor test results show that the ZESRC can switch modes automatically in response to temperature changes, suiting different environmental conditions. The outdoor spectral durability tests for ZESRC are illustrated in Fig. 15. The ZESRC operates its cooling and heating cycles with intelligent mode transition without any energy consumption, supporting smart, adaptive thermal management for all-season, and real-world use.

### 3.4.3 *Net cooling/heating power calculation*

During outdoor testing, our ZESRC showed outstanding thermal management, targeting optimal performance under theoretical and ideal conditions. As illustrated in Fig. 4(d), we have calculated the trends of net cooling power as a function of temperature difference under various nonradiative heat transfer coefficients ($h_c$), as detailed in Note 3 in the Appendix section. In cooling mode, when the cooler's surface temperature matched the ambient, it reached a peak net cooling power of 127.99 $\mathrm{W/m^2}$, indicating a high level of performance in line with the field's advanced standards. Theoretically, with $h_c$ values of 0, 6, and 12, the projected maximum daytime temperature reductions were 30.8°C, 12.0°C, and 7.6°C, respectively. Discrepancies between on-site results and theoretical predictions may stem from factors like higher humidity and unavoidable thermal losses. Figure 4(e) presents the variation in heating power with temperature difference under different nonradiative heat transfer coefficients ($h_c$) during daytime heating mode. Theoretically, the ZESRC could attain a maximum heating power of 201.39 $\mathrm{W/m^2}$ when the surface temperature of the ZESRC matched the ambient temperature in the heating mode.

### 3.5 Architectural Energy Saving Simulation Prediction

To predict the energy-saving potential of our ZESRC for buildings, we used EnergyPlus (version 22.2), a commercial building energy simulation software, and detailed simulation calculations can be found in Note 4 in the Appendix section. The simulations were based on the optical properties of the ZESRC and real weather data from China to calculate the energy-saving effects for heating only, cooling only, and dual-mode (ZESRC) building envelopes throughout all 12 months of the year. We examined cities across different climatic zones in China. Figures 5(a) and 5(b) illustrate the energy-saving predictions for heating-only and cooling-only modes, respectively. The data from the aforementioned figures clearly demonstrate a strong dependence of the energy-saving effects of the heating and cooling modes on latitude. The heating mode is only applicable in the northern regions where there is a higher demand for heating due to its high solar absorption and low-infrared radiation characteristics, which can even result in negative energy savings in the warmer southern regions where the heat load is lower. Conversely, the cooling mode is only suitable for the southern regions with higher cooling demands; similarly, the exclusive use of radiative cooling technology in the north, where the cooling load is smaller, can have an adverse effect on energy savings. Although the single cooling mode showcases powerful all-weather cooling capabilities, as the latitude increases, the demand for cooling transitions from high to low, and the costs of cooling gradually become offset by the escalating heating costs. The single heating mode suffers from the same drawback, highlighting the limitations of a singular-mode approach. Figure 5(c) illustrates that, in comparison with single-mode devices, our ZESRC's dual-mode effectively resolves the latitude-dependent energy-saving issues previously outlined, affirming its successful integration of the advantages of both heating and cooling modes. The ZESRC's dual-mode exhibits notable energy-saving benefits across almost all regions in China. We calculated the annual energy savings in $\mathrm{MJ/m^2}$ [shown in Fig. 5(d)] for

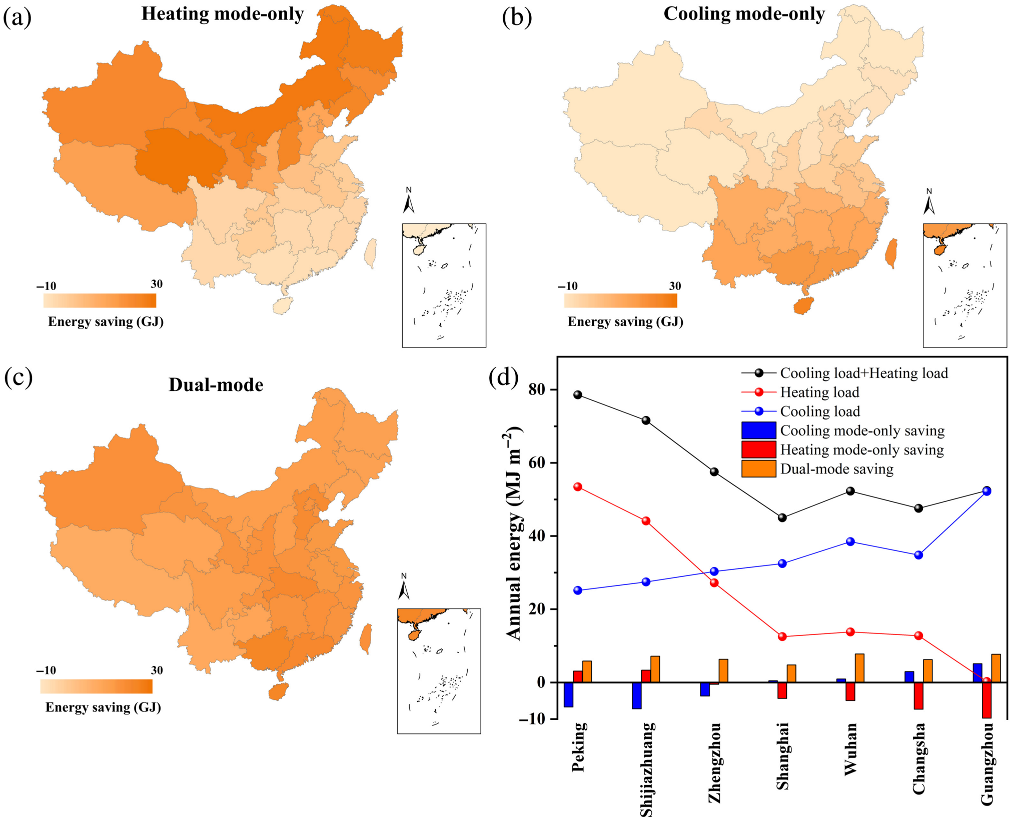

**Fig. 5** Annual energy-saving modes correspond to different climate zones in China under different modes. (a) Energy-saving map under heating-only mode. (b) Energy-saving map under cooling-only mode. (c) A dual-mode energy-saving map specifically aligned with the ZESRC. (d) Energy load and annual average energy savings in different cities under different modes.

buildings in seven Chinese cities representing different climate zones: Beijing, Shijiazhuang, Zhengzhou, Shanghai, Wuhan, Changsha, and Guangzhou. Taking Wuhan as an example, our ZESRC can save an average of 7.76 $\mathrm{MJ/m^2}$ annually, which is equivalent to 14.8% of the total annual energy consumption of air conditioning systems, substantially surpassing the energy savings of 0.94 $\mathrm{MJ/m^2}$ in the single cooling mode and $-4.97$ $\mathrm{MJ/m^2}$ in the heating mode.

## 4 Conclusions

In conclusion, our study has led to the development of a ZESRC, presenting a novel solution to reduce energy consumption in buildings and combat the climate crisis. Utilizing a simple morphology-driven strategy, the ZESRC harnesses the inherent thermal expansion coefficient differences between materials to intelligently switch between cooling mode ($\alpha_{0.28\text{ to }0.78\ \mu\mathrm{m}}$ of 0.2% and $\varepsilon_{8\text{ to }13\ \mu\mathrm{m}}$ of 96.2%) and heating mode ($\alpha_{0.28\text{ to }0.78\ \mu\mathrm{m}}$ of 33.2% and $\varepsilon_{8\text{ to }13\ \mu\mathrm{m}}$ of 0.3%) at any preset temperature point. Field studies have demonstrated ZESRC's excellent adaptive thermal management performance, with the use of ZESRC reducing summer maximum temperatures by 7.1°C and increasing winter maximum temperatures by 7.5°C compared to ambient temperatures. Furthermore, an energy-saving map was developed for various climate zones in China, revealing that the ZESRC outperforms devices that merely utilize solar heating or radiative cooling. The ZESRC offers an average energy savings of 14.3% in total building heating and cooling energy consumptions. These findings highlight the ZESRC's potential for net-zero energy consumption and a substantial contribution to energy conservation globally. Addressing the growing energy demand, the ZESRC is a promising advancement toward the net-zero carbon goal by 2050. Future research will aim to optimize the ZESRC's design for improved performance and test its application across different global climates and buildings.

## 5 Appendix

### 5.1 Figure Descriptions

This appendix provides detailed descriptions of Figures 6–15, showcasing key experimental data and illustrations used in our study.

Figure 6 demonstrates the linear thermal expansion coefficients of PE films and copper foils as a function of temperature, revealing the relationship between material thermal expansion properties and temperature. This is crucial for understanding the working principle of temperature-sensitive actuators.

Figure 7 shows the bending performance of temperature-sensitive actuators with different PE film thicknesses. By keeping the copper foil thickness constant, the study investigates the impact of ambient temperature changes (15°C to 35°C) on the bending angles of actuators with varying PE thicknesses.

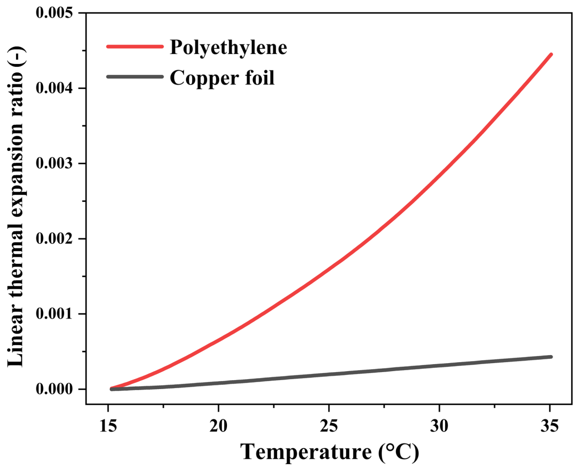

**Fig. 6** Changes in the linear thermal expansion coefficient of PE film and copper foil with temperature.

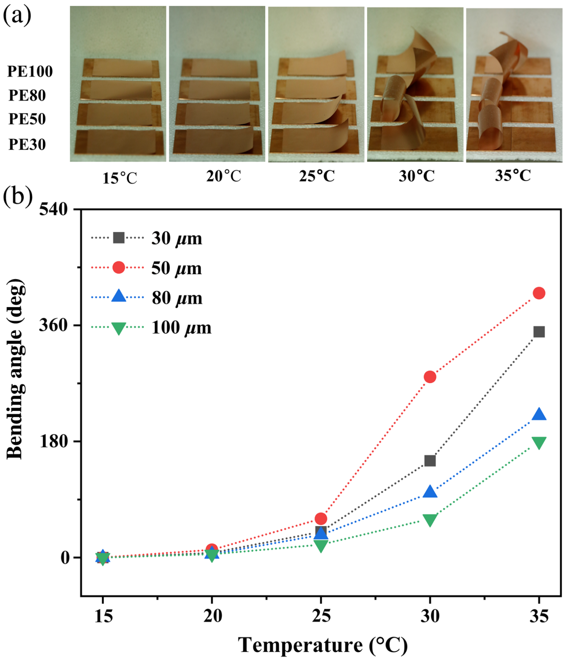

**Fig. 7** Bending performance of the temperature-sensitive actuator under different PE film thicknesses (with a fixed copper foil thickness of 20 μm). (a) Optical images of the temperature-sensitive actuator as the environmental temperature changes (15°C to 35°C). (b) The bending angle performance of the temperature-sensitive actuator as the environmental temperature changes, with changing PE thicknesses of 30, 50, 80, and 100 μm, respectively.

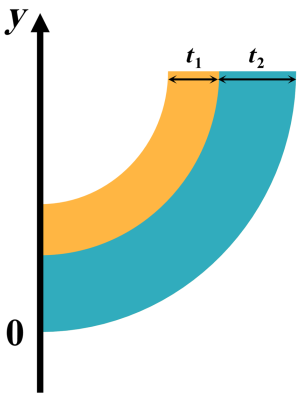

**Fig. 8** Diagram of a temperature-sensitive actuator in a balanced state.

Figure 8 presents a schematic of a temperature-sensitive actuator in equilibrium, explaining how the actuator achieves balance at different temperatures, enabling temperature-driven switching mechanisms.

Figure 9 displays an actual device used for outdoor testing, providing a visual understanding of the device design and its application in real-world scenarios.

Figure 10 depicts the size distribution of zirconia particles, essential for understanding how particles in the radiative cooling layer affect the material's scattering and absorption properties.

Figure 11 illustrates the effect of different mass ratios on the spectral performance of radiative coolers, especially the variations in solar reflectance and infrared emissivity with changes in the PMMA to $ZrO_2$ mass ratio.

Figure 12 shows the variation of solar reflectance with thickness under a controlled mass ratio of 1:1, demonstrating the influence of thickness on solar reflectance performance.

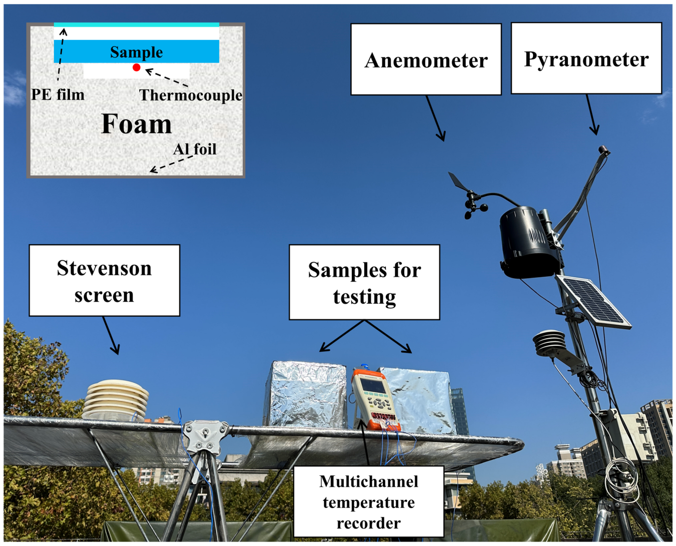

**Fig. 9** Picture of the actual device used in outdoor testing.

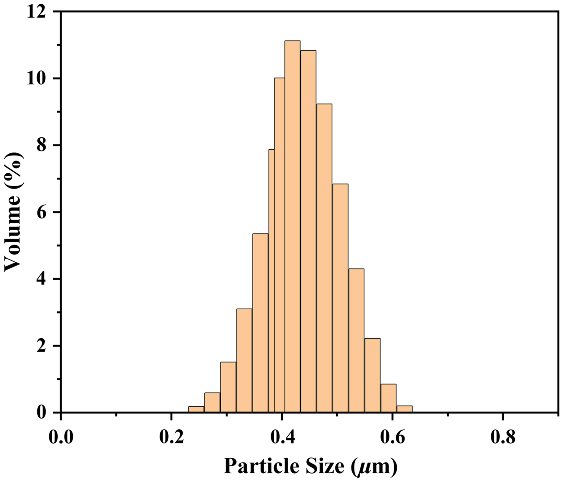

**Fig. 10** Particle size distribution of zirconia.

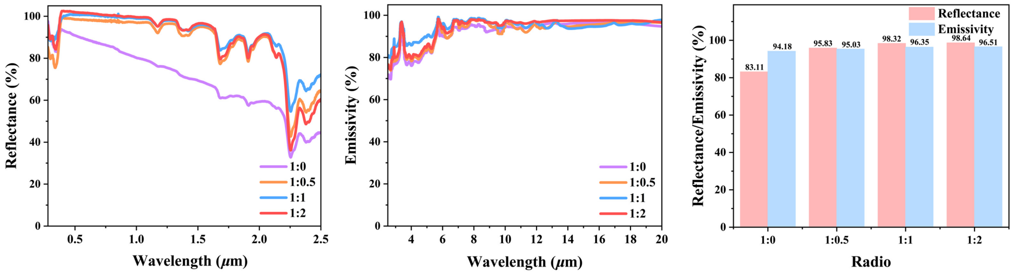

(a) (b) (c)

**Fig. 11** Impact of different mass ratios on the spectra in radiative cooler. (a) Variation of solar reflectance with PMMA:$ZrO_2$ mass ratio. (b) Variation of infrared emissivity with PMMA:$ZrO_2$ mass ratio. (c) Reflectance and emissivity at different mass ratios. This study investigates the spectral performance of PMMA and $ZrO_2$ at different mass ratios. As shown in (a), the solar reflectance in the solar light band gradually increases from 83.11% to 98.64% with the increase in the proportion of $ZrO_2$. As illustrated in (b), the infrared emissivity also slightly increases from 94.18% to 96.54% with the increasing ratio. In conclusion, when the ratio is 1:1 and 1:2, the radiative cooler achieves optimal performance in terms of both solar reflectance and infrared emissivity.

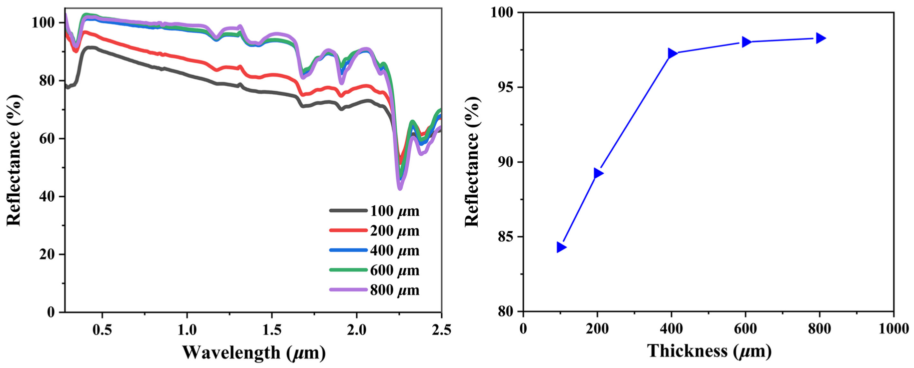

(a) (b)

**Fig. 12** Under the condition of a controlled mass ratio of 1:1, the variation of solar reflectance with thickness. (a) Solar reflectance spectra corresponding to different thicknesses. (b) Solar reflectance variation with thickness. The data graph indicates that the solar reflectance gradually increases with thickness until it reaches a thickness of 400 $\mu$m, after which the solar reflectance remains essentially constant.

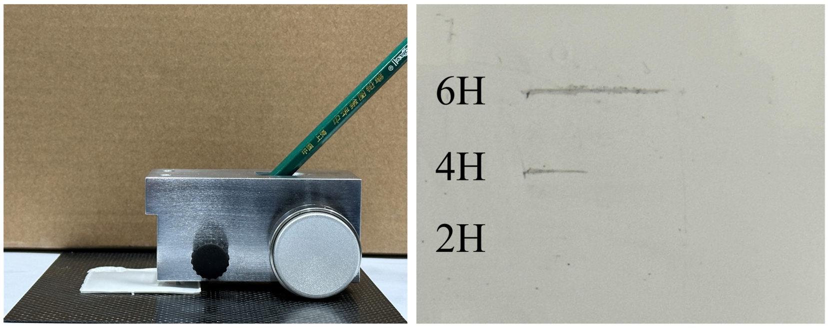

(a) (b)

**Fig. 13** Pencil hardness test for the radiative cooler. (a) The mass of the weight is 500 g. (b) Radiative cooler tested under different pencil hardness conditions.

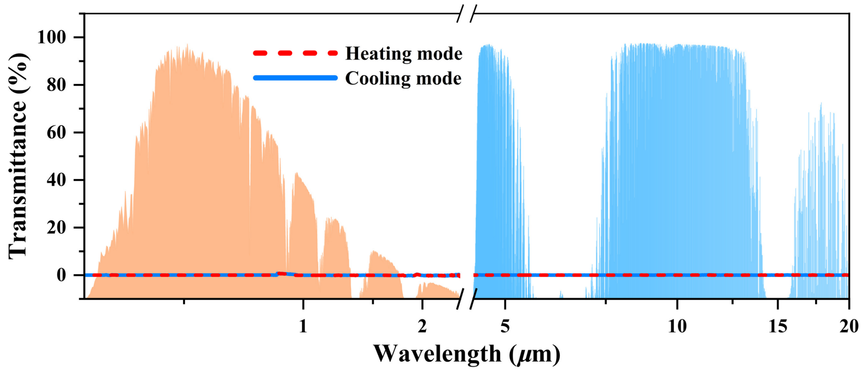

**Fig. 14** Spectral transmittance of ZESRC in heating mode and cooling mode.

Figure 13 assesses the physical stability of radiative coolers through pencil hardness tests, showcasing the surface wear resistance of radiative coolers under different pencil hardness conditions.

Figure 14 reveals the spectral transmittance of ZESRC in heating and cooling modes, showing its ability to transmit and block spectral energy in different modes.

Figure 15 evaluates the anti-aging properties of ZESRC through spectral aging performance tests, showing changes in UV-VIS absorption rates and atmospheric window infrared emission rates after 180 days of outdoor exposure, indicating good spectral stability.

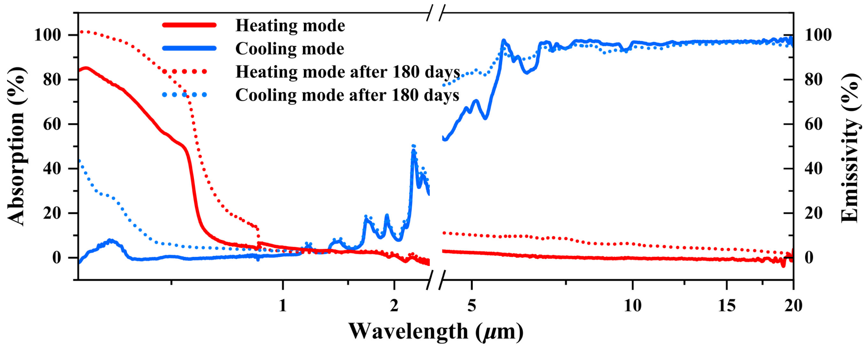

**Fig. 15** Spectral aging performance testing of ZESRC. After 180 days of outdoor exposure, ZESRC's antiaging properties were evaluated using a spectrometer. The cooling mode of ZESRC exhibited a slight increase in spectral absorptance in the UV-VIS light band, with the solar light band absorptance increasing from the original 2.03% to 6.38%. In the atmospheric window infrared emission band, however, its spectral emissivity showed almost no change, decreasing slightly from 96.17% to 94.18%. In heating mode, both the absorptance in the UV-VIS band and the infrared emissivity saw a slight increase, with the solar light band absorptance rising from 20.14% to 33.12%, and the atmospheric window emissivity increasing from 0.30% to 5.78%. These findings suggest that ZESRC demonstrates robust spectral aging resistance.

The above figures provide critical experimental data and insights that form the foundation of our work.

## 5.2 Note 1. Bending Mechanism and Theoretical Calculation of the Temperature-Sensitive Actuating Layer

The temperature-sensitive actuating layer adheres at a preset temperature point, such as around 20°C typically in laboratory conditions. At this state, there is no thermal stress within the temperature-sensitive actuating layer, allowing it to maintain a flat configuration. Due to the actuator's thinness, the temperature distribution within the temperature-sensitive actuating layer is assumed to be uniform in a state of thermal equilibrium. As the ambient temperature increases, so does the temperature of the temperature-sensitive actuating layer. When the ambient temperature reaches 35°C, in thermal equilibrium, the temperature of the temperature-sensitive actuating layer will also be 35°C. The temperature-sensitive actuating layer consists of a thermally expansible sensitive layer (PE) and a thermally inert layer (copper foil). During the heating process from 15°C to 35°C, the PE film, having a relatively higher thermal expansion rate, tends to expand along its length. In contrast, the copper foil expands less due to its lower thermal expansion rate. With increasing temperature, the bilayer structure undergoes bending due to thermal stress caused by thermal mismatch. During the cooling process from 35°C to 15°C, the previously expanded PE layer gradually contracts to match the copper foil layer, causing the overall bilayer structure to progressively flatten from its bent state. This behavior illustrates the temperature-responsive nature of the actuating layer, responding to changes in ambient temperature by altering its physical configuration.

To fully understand the steady-state bending behavior of the temperature-sensitive actuating layer, we conducted a theoretical analysis. Figure 8 illustrates the schematic of the temperature-sensitive actuator in its balanced state. Constraints are applied to the temperature-sensitive actuating layer, with displacement constraints set at the left end of the structure. In the stable bent state, the strain distribution within the system can be divided into uniform strain components and bending strain components. Within each layer, the relationship between the normal stress and the total strain is derived using Hooke's law:[47,48]

$$\sigma = E'(\varepsilon - v'\varepsilon^0), \tag{1}$$

$E' = E/(1 - v^2)$. $E$ represents the Young's modulus, and $v$ denotes the Poisson's ratio. $v' = 1 + v$; $\varepsilon^0$ refers to the original strain in both the PE layer and the copper foil layer.

In the temperature-sensitive actuating layer, the total strain $\varepsilon$ is linearly proportional to the $y$ coordinate as follows:

$$\varepsilon = \frac{y - y_a}{R} + b. \tag{2}$$

In this equation, $y_a$ represents the $y$ coordinate at the position where the bending strain component is zero; $R$ is the radius of curvature of the bilayer structure; and $b$ is the component of uniform strain. By substituting Eq. (2) into Eq. (1), an expression for the normal stress $\sigma$ can be derived

$$\sigma = E'\left(\frac{y - y_a}{R} + b - v'\varepsilon^0\right). \tag{3}$$

In this formula, there are three unknown parameters, including $y_a$, $b$, and $R$. When the temperature-sensitive actuating layer is in a balanced state, the bending stress, uniform strain, and bending moment in this state should all be zero. From this, the following three equilibrium equations can be established as follows:

$$\sum_{i=1}^{2}\int_{y_{i-1}}^{y_i} E_i'\frac{(y - y_a)}{R}\mathrm{d}y = 0, \tag{4}$$

$$\sum_{i=1}^{2}\int_{y_{i-1}}^{y_i} E_i'(b - v_i'\varepsilon_i^0)\mathrm{d}y = 0, \tag{5}$$

$$\sum_{i=1}^{2}\int_{y_{i-1}}^{y_i} E_i'\left(\frac{y - y_a}{R} + b - v_i'\varepsilon_i^0\right)(y - y_a)\mathrm{d}y = 0. \tag{6}$$

During the integration process, $y_0$, $y_1$, and $y_2$ are substituted with 0, $t_1$, and $t_1 + t_2$, respectively. As our primary focus is to explore the relationship of the bending radius $R$, the expression for $R$ can only be obtained after solving the aforementioned three equilibrium equations:

$$R = \frac{(E_1')^2 t_1^4 + (E_2')^2 t_2^4 + 2E_1'E_2' t_1 t_2 (2t_1^2 + 2t_2^2 + 3t_1 t_2)}{6E_1'E_2' t_1 t_2 (t_1 + t_2)(v_1'\varepsilon_1^0 - v_2'\varepsilon_2^0)}. \tag{7}$$

In this context, the subscripts 1 and 2, respectively, represent the PE layer and the copper foil layer; $t$ denotes their thicknesses. Finally, we can calculate the bending angle using the following formula:

$$\theta = 360\frac{l}{2\pi R} = \frac{1080 l E_1'E_2' t_1 t_2 (t_1 + t_2)(v_1'\varepsilon_1^0 - v_2'\varepsilon_2^0)}{\pi[(E_1')^2 t_1^4 + (E_2')^2 t_2^4 + 2E_1'E_2' t_1 t_2 (2t_1^2 + 2t_2^2 + 3t_1 t_2)]}. \tag{8}$$

In this description, $l$ represents the length of the temperature-sensitive actuating layer. $\varepsilon_1^0$ is the initial strain in the original PE layer, and $\varepsilon_2^0$ is the initial strain in the copper foil layer. These can be calculated based on the thermal expansion coefficients and temperature difference as shown in Fig. 6.

### 5.3 Note 2. The Definition of Average Reflectance and Emissivity

The average solar reflectance ($\overline{R}_{\mathrm{solar}}$) denoted as[15,16]

$$\overline{R}_{\mathrm{solar}} = \frac{\int_{0.3\ \mu\mathrm{m}}^{2.5\ \mu\mathrm{m}} I_{\mathrm{solar}}(\lambda) R_{\mathrm{solar}}(\lambda)\mathrm{d}\lambda}{\int_{0.3\ \mu\mathrm{m}}^{2.5\ \mu\mathrm{m}} I_{\mathrm{solar}}(\lambda)\mathrm{d}\lambda}. \tag{9}$$

In Eq. (9), $\lambda$ represents the solar light band from 0.3 to 2.5 $\mu$m, $I_{\mathrm{solar}}(\lambda)$ is the normalized ASTM G173 global solar intensity spectrum, and $R_{\mathrm{solar}}(\lambda)$ is the spectral reflectance of the device.

The average emissivity in the long-wave infrared atmospheric transmission window, $\bar{\varepsilon}_{\mathrm{LWIR}}$ is defined as

$$\bar{\varepsilon}_{\mathrm{LWIR}} = \frac{\int_{8\ \mu\mathrm{m}}^{13\ \mu\mathrm{m}} I_{BB}(T, \lambda)\varepsilon_{\mathrm{LWIR}}(\lambda)\mathrm{d}\lambda}{\int_{8\ \mu\mathrm{m}}^{13\ \mu\mathrm{m}} I_{BB}(T, \lambda)\mathrm{d}\lambda}. \tag{10}$$

In Eq. (10), $I_{\mathrm{BB}}(T,\lambda)=\frac{2hc^2}{\lambda^5}\frac{1}{e^{hc/\lambda k_B T}-1}$ is the spectral radiation intensity of a black body at temperature $T$ (assumed to be 25°C) as defined by Planck's law. $h$ is the Planck's constant, $k_B$ is the Boltzmann's constant, $c$ is the speed of light in a vacuum, and $\varepsilon_{\mathrm{LWIR}}(\lambda)$ is the emissivity of the device in the atmospheric window range of 8 to 13 $\mu$m.

The emissivity of the material $\varepsilon(\lambda)$ is given by Kirchoff's law of thermal radiation:

$$\varepsilon(\lambda)=\alpha(\lambda)=1-\tau(\lambda)-R(\lambda). \tag{11}$$

In Eq. (11), $\alpha(\lambda)$ is the absorption rate, $\tau(\lambda)$ is the transmission rate, and $R(\lambda)$ is the reflectance rate.

## 5.4 Note 3. The Theoretical Calculation of Net Cooling/Heating Power

$$P_{\mathrm{net}}(T)=P_{\mathrm{rad}}(T)-P_{\mathrm{Sun}}-P_{\mathrm{atm}}(T_{\mathrm{atm}})-P_{\mathrm{cond+conv}}(T,T_{\mathrm{atm}}), \tag{12}$$

$$P_{\mathrm{rad}}(T)=A\int \mathrm{d}\Omega\,\cos\theta\int_0^\infty \mathrm{d}\lambda I_{BB}(T,\lambda)\varepsilon(\lambda,\theta), \tag{13}$$

$$P_{\mathrm{Sun}}=\int_0^\infty I_{\mathrm{solar}}(\lambda)(1-R_{\mathrm{solar}}(\lambda))\mathrm{d}\lambda, \tag{14}$$

$$P_{\mathrm{atm}}(T_{\mathrm{atm}})=A\int \mathrm{d}\Omega\,\cos\theta\int_0^\infty \mathrm{d}\lambda I_{BB}(T_{\mathrm{atm}},\lambda)\varepsilon(\lambda,\theta)\varepsilon_{\mathrm{atm}}(\lambda,\theta), \tag{15}$$

$$P_{\mathrm{cond+conv}}=h_c(T_{\mathrm{amb}}-T). \tag{16}$$

In the context of a ZESRC operating in cooling mode, $P_{\mathrm{net}}(T)$ denotes the net cooling power of the device, $P_{\mathrm{rad}}$ is the power radiated outward by the device, $P_{\mathrm{Sun}}$ stands for the power absorbed from solar radiation by the device, $P_{\mathrm{atm}}$ represents the power absorbed from atmospheric radiation by the device, and $P_{\mathrm{cond+conv}}$ signifies the power from nonradiative heat exchange processes, such as conduction and convection. The terms $T$ and $T_{\mathrm{atm}}$ correspond to the device temperature and the ambient temperature, respectively.

For Eq. (12), under the condition that the temperature ($T$) of the ZESRC reaches a steady state, the aforementioned parts achieve thermal equilibrium. In Eq. (13), $\int \mathrm{d}\Omega\,\cos\theta$ is the radiation angle integral over the hemispherical space.

In Eq. (15), the term $\varepsilon_{\mathrm{atm}}(\lambda,\theta)=1-\tau_{\mathrm{atm}}(\lambda,\theta)=1-\tau(\lambda)^{1/\cos\theta}$ denotes the angle-dependent spectral emissivity of the atmosphere. Here $\tau_{\mathrm{atm}}(\lambda,\theta)=\tau(\lambda)^{1/\cos\theta}$ represents the angle-dependent atmospheric transmittance, and $\tau(\lambda)$ indicates the atmospheric transmittance in the zenith direction.

Regarding Eq. (16), $h_c$ is the nonradiative heat exchange coefficient resulting from the combined conduction and convection heat exchange between the device and the surrounding air. Its range can be restricted between 0 and 12 $\mathrm{W/m^2/K}$.

## 5.5 Note 4. Energy-Saving Simulation

We used EnergyPlus software (version 22.2) to simulate the energy-saving potential of the ZESRC we prepared. Based on the commercial reference building model from the U.S. Department of Energy, we established a typical midrise apartment building with a total area of 1567 $\mathrm{m^2}$. We assigned the exterior wall materials with the dual-mode spectral switching characteristics of ZESRC, setting the switching temperature point at 20°C. We set the cooling setpoint at 26°C and the heating setpoint at 18°C to simulate the building's annual energy consumption under different climatic conditions in China and used an ideal air conditioning system to output heating and cooling loads. The Chinese weather data required for the simulation came from the official website of EnergyPlus.

---

## Disclosures

The authors declare no competing financial interests.

## Code and Data Availability

All data in support of the findings of this paper are available within the article or as supplementary material.

## Author Contributions

C.C. and X.X. conceived the idea and designed the experiments. J.H., R.S., B.L., and H.H. performed the experiment and simulation. C.C., Y.P., and Z.X. completed the writing of this paper. All authors have read and agreed to the published version of the manuscript.

## Acknowledgments

This work was supported by Zibo Key Research and Development Project (Grant Nos. 2020XCCG0106 and 2021SNPT0004).

## References

1. J. E. Tierney et al., "Glacial cooling and climate sensitivity revisited," *Nature* **584**(7822), 569–573 (2020).
2. L. Zhao et al., "Strong contributions of local background climate to urban heat islands," *Nature* **511**(7508), 216–219 (2014).
3. A. Perera et al., "Quantifying the impacts of climate change and extreme climate events on energy systems," *Nat. Energy* **5**(2), 150–159 (2020).
4. Y. Ke et al., "Smart windows: electro-, thermo-, mechano-, photochromics, and beyond," *Adv. Energy Mater.* **9**(39), 1902066 (2019).
5. A. Inayat and M. Raza, "District cooling system via renewable energy sources: a review," *Renew. Sustain. Energy Rev.* **107**, 360–373 (2019).
6. M. C. Huang et al., "Scalable multifunctional radiative cooling materials," *Prog. Mater. Sci.* **137**, 101144 (2023).
7. M. M. Hossain and M. Gu, "Radiative cooling: principles, progress, and potentials," *Adv. Sci.* **3**(7), 1500360 (2016).
8. B. Zhao et al., "Radiative cooling: a review of fundamentals, materials, applications, and prospects," *Appl. Energy* **236**, 489–513 (2019).
9. A. P. Raman et al., "Passive radiative cooling below ambient air temperature under direct sunlight," *Nature* **515**(7528), 540–544 (2014).
10. D. Chae et al., "Spectrally selective inorganic-based multilayer emitter for daytime radiative cooling," *ACS Appl. Mater. Interfaces* **12**(7), 8073–8081 (2020).
11. E. Rephaeli, A. Raman, and S. Fan, "Ultrabroadband photonic structures to achieve high-performance daytime radiative cooling," *Nano Lett.* **13**(4), 1457–1461 (2013).
12. A. Leroy et al., "High-performance subambient radiative cooling enabled by optically selective and thermally insulating polyethylene aerogel," *Sci. Adv.* **5**(10), eaat9480 (2019).
13. X. Liu et al., "Hierarchically superhydrophobic stereo-complex poly (lactic acid) aerogel for daytime radiative cooling," *Adv. Funct. Mater.* **32**(46), 2207414 (2022).
14. J. Wang et al., "Optical design of silica aerogels for on-demand thermal management," *Adv. Funct. Mater.* **33**(32), 2300441 (2023).
15. T. Wang et al., "A structural polymer for highly efficient all-day passive radiative cooling," *Nat. Commun.* **12**(1), 365 (2021).
16. J. Mandal et al., "Hierarchically porous polymer coatings for highly efficient passive daytime radiative cooling," *Science* **362**(6412), 315–319 (2018).
17. Z. Cheng et al., "Efficient radiative cooling coating with biomimetic human skin wrinkle structure," *Nano Energy* **89**, 106377 (2021).
18. T. Li et al., "A radiative cooling structural material," *Science* **364**(6442), 760–763 (2019).
19. W. Zhu et al., "Large-scale industry-compatible sub-ambient radiative cooling pulp," *Cell Rep. Phys. Sci.* **3**(11), 101125 (2022).
20. K. Zhang et al., "A zero-energy, zero-emission air conditioning fabric," *Adv. Sci.* **10**(11), 2206925 (2023).
21. H. Yuan et al., "Scalable fabrication of dual-function fabric for zero-energy thermal environmental management through multiband, synergistic, and asymmetric optical modulations," *Adv. Mater.* **35**(18), 2209897 (2023).
22. S. Zeng et al., "Hierarchical-morphology metafabric for scalable passive daytime radiative cooling," *Science* **373**(6555), 692–696 (2021).
23. R. Liu et al., "Green-manufactured and recyclable coatings for subambient daytime radiative cooling," *ACS Appl. Mater. Interfaces* **14**(41), 46972–46979 (2022).

24. X. Li et al., "Ultrawhite $BaSO_4$ paints and films for remarkable daytime subambient radiative cooling," *ACS Appl. Mater. Interfaces* **13**(18), 21733–21739 (2021).
25. Y. Zhang et al., "Effective radiative cooling with $ZrO_2$/PDMS reflective coating," *Sol. Energy Mater. Sol. Cells* **229**, 111129 (2021).
26. Z. Xi et al., "All-day freshwater harvesting by selective solar absorption and radiative cooling," *ACS Appl. Mater. Interfaces* **14**(22), 26255–26263 (2022).
27. Y. Zhang et al., "Atmospheric water harvesting by large-scale radiative cooling cellulose-based fabric," *Nano Lett.* **22**(7), 2618–2626 (2022).
28. Y. Peng and Y. Cui, "Advanced textiles for personal thermal management and energy," *Joule* **4**(4), 724–742 (2020).
29. X. Wu et al., "An all-weather radiative human body cooling textile," *Nat. Sustain.* **6**, 1446–1454 (2023).
30. Z. Xia et al., "Thermoelectric generator using space cold source," *ACS Appl. Mater. Interfaces* **11**(37), 33941–33945 (2019).
31. S. Assawaworrarit, Z. Omair, and S. Fan, "Nighttime electric power generation at a density of 50 $mW/m^2$ via radiative cooling of a photovoltaic cell," *Appl. Phys. Lett.* **120**(14), 143901 (2022).
32. Y. Tu et al., "Antireflection and radiative cooling difunctional coating design for silicon solar cells," *Opt. Express* **31**(14), 22296–22307 (2023).
33. K. W. Lee et al., "Visibly clear radiative cooling metamaterials for enhanced thermal management in solar cells and windows," *Adv. Funct. Mater.* **32**(1), 2105882 (2022).
34. S. Wijesuriya et al., "Potential energy savings benefits and limitations of radiative cooling coatings for U.S. Residential Buildings," *J. Clean. Prod.* **379**, 134763 (2022).
35. J. Mandal et al., "Paints as a scalable and effective radiative cooling technology for buildings," *Joule* **4**(7), 1350–1356 (2020).
36. Y. Ke et al., "On-demand solar and thermal radiation management based on switchable interwoven surfaces," *ACS Energy Lett.* **7**(5), 1758–1763 (2022).
37. X. Li et al., "Integration of daytime radiative cooling and solar heating for year-round energy saving in buildings," *Nat. Commun.* **11**(1), 6101 (2020).
38. S. Y. Heo, G. J. Lee, and Y. M. Song, "Heat-shedding with photonic structures: radiative cooling and its potential," *J. Mater. Chem. C* **10**(27), 9915–9937 (2022).
39. M. Liu et al., "Continuous photothermal and radiative cooling energy harvesting by $VO_2$ smart coatings with switchable broadband infrared emission," *ACS Nano* **17**(10), 9501–9509 (2023).
40. K. Tang et al., "Temperature-adaptive radiative coating for all-season household thermal regulation," *Science* **374**(6574), 1504–1509 (2021).
41. S. Wang et al., "Scalable thermochromic smart windows with passive radiative cooling regulation," *Science* **374**(6574), 1501–1504 (2021).
42. S. Liu et al., "Self-densified optically transparent $VO_2$ thermochromic wood film for smart windows," *ACS Appl. Mater. Interfaces* **13**(19), 22495–22504 (2021).
43. Y. Qiu et al., "Dielectric elastomer artificial muscle: materials innovations and device explorations," *ACC. Chem. Res.* **52**(2), 316–325 (2019).
44. J. Huang et al., "Effects of humidity, aerosol, and cloud on subambient radiative cooling," *Int. J. Heat Mass Transf.* **186**, 122438 (2022).
45. A. Aili et al., "Selection of polymers with functional groups for daytime radiative cooling," *Mater. Today Phys.* **10**, 100127 (2019).
46. P. Liu et al., "Functional radiative cooling: basic concepts, materials, and best practices in measurements," *ACS Appl. Electron. Mater.* **5**(11), 5755–5776 (2023).
47. C.-H. Hsueh, "Modeling of elastic deformation of multilayers due to residual stresses and external bending," *J. Appl. Phys.* **91**(12), 9652–9656 (2002).
48. J. Chai et al., "Thermoregulatory clothing with temperature-adaptive multimodal body heat regulation," *Cell Rep. Phys. Sci.* **3**(7), 100958 (2022).

Biographies of the authors are not available.